Nonlinear buckling and folding analysis of a storable tubular ultrathin boom for nanosatellites

Daniele Barbera[1], Susanna Laurenzi[2*]

[1] Department of Mechanical and Aerospace Engineering, University of Strathclyde, 75 Montrose Street, Glasgow G1 1XJ, UK

[2] Department of Astronautic Electrical and Energy Engineering, Sapienza University of Rome, Via Salaria 851-881, 00138 Rome, Italy

Abstract

In this work we investigated the stability behavior and the folding capability of an ultrathin tubular composite boom with C-cross section to be used in nanosatellites applications. A nonlinear buckling analysis was performed using the Riks method, adopting a perturbed finite element model to study the influence of the unavoidable geometrical variations of the boom thickness, arising from the composite manufacturing processes, on the stability behavior of the tubular structure. The effect of several levels of geometrical imperfection on the buckling behavior was analyzed. The minimum coil radius that can be used for a safe storage the boom was determined by quasi-static explicit analysis. The boom folding process was considered as formed by two sequential steps, the flattening and the coiling. The stress fields associated with both steps were investigated.

Keywords: deployable structures, ultrathin composite, buckling analysis, finite element method

[*] *Corresponding author.* Tel.: +39 06 49 919 756; Fax: +39 06 49 919 757.

E-mail address: susanna.laurenzi@uniroma1.it (S. Laurenzi)

1. Introduction

Storable tubular extensible members (STEMs) have been widely investigated for many years as technological solution for numerous space applications [1-5]. STEMs are considered for stabilization systems via gravity gradient in low orbit spacecrafts [6, 7], self-deployable antennas [8], and deployable booms for solar sails [9, 10]. Their peculiarity is the capability to change the configuration from a packed arrangement, which is suitable for the launch phase, to a large-scale deployable configuration once in orbit.

Cylindrical composite booms are the simplest deployable structures among STEMs, using the strain energy stored during the folding process to provide the motive force for deployment. In these cylindrical systems, the folding and deployment mechanisms have low complexity, and the presence of external energy sources such as motors is not necessary. The lack of these additional elements leads to a significant weight saving and a smaller required volume for the structure. These advantages can be exploited in the design of micro- and nanosatellites, allowing them to be equipped with tip payloads. For example, cylindrical booms may be used to position sensitive instruments far from the interferences caused by the satellite subsystems. On the other hand, despite their potential uses, the knowledge of the real structural behavior of deployable composite booms is not sufficiently established. In fact, Schenk *et al.* recently highlighted that the large research efforts on deployable structures are not compensated by an appropriate technology readiness level [11]. An accurate *ad hoc* design of the deployable structure is necessary to avoid its failure during folding, stowage, deployment and operative life.

Cylindrical composite booms suffer from bending and torsional stiffness, as well as buckling instability. Moreover, these structures are realized using ultrathin laminates to make them foldable. The use of ultrathin composites jeopardizes the application of traditional failure criteria, as they lack the accuracy for bending and axial-bending interactions [12]. In addition, in cylindrical composite booms, the cross-sectional shape plays an important role in the definition of the loading limits. Different types of cross-sections were studied in the literature, including Y-shape, single STEM, interlocked bi-STEM omega shape [10], and double omega cross-section [3, 9, 13, 14].

In this work, we investigate the buckling behavior and the structural integrity under folding process of a boom with C-open cross-section, having radius of 10 mm and a 2-mm-wide opening [15-17]. The C-open cross-section offers several advantages with respect to the above mentioned cross-sectional shapes. First, it has a cost-efficient manufacturing due to its geometry of low complexity. In addition, the simplicity of the shape allows to reduce the formation of areas with high stress concentrations due to the packaging. We use a nonlinear analysis with the Riks method to estimate the critical load of the composite boom and the effects of random geometry imperfections on the boom stability behavior. In particular, we study how the geometry imperfections, inherently related to the manufacturing, throughout the structure thickness influence the boom stability behavior with respect to the critical load. In addition, we study the structural integrity of the boom during the folding process using quasi-static explicit analysis. We determine the minimum coil radius that can be achieved during the rolling process without failure of the laminate, and the stress fields related to the flattening and coiling steps.

2. Finite element modelling

2.1 FEM models

Numerical analyses were performed in double precision using the finite element method (FEM) by the commercial code ABAQUS 6.12. Two different FEM models were realized to perform the buckling and folding analyses, respectively. In both cases, the boom geometry was discretized by implicit/explicit shell reduced-integration elements (S4R). This class of elements allows considering only the linear part of the nodal incremental displacement, thus reducing widely the computational cost. The nonlinear part is represented by hourglass modes, which can produce an excessive mesh deformation during the computational simulation [18]. In order to avoid this problem, the hourglass control method is in general adopted.

Fig. 1 shows a schematic of the constraints used for the linear and nonlinear buckling analysis: one extremity of the boom was constrained in the x-y plane translations and z rotation, whereas the other extremity had also the z translation fixed. The axial load was transferred to the structure using a master node positioned in the center of the section and connected to the slave nodes located around the contour of the C-section, as shown in the detailed view in Fig. 1. The number of elements was set using a mesh sensitivity analysis. The analysis was based on the results of the linear buckling, in particular, comparing the critical loads determined with different number of elements. The results of this analysis are summarized in Table 1, where it can be observed that mesh 2 is the discretization that carries out a stable result with the smallest number of elements, and therefore could be selected for the numerical analyses. However, we noted that, in order to guarantee the stability of the Riks analysis, a mesh with the element aspect ratio approaching the unity was necessary. For this reason, we used mesh 3 for the analyses, which presents a square elements and the computational time is still acceptable. Fig. 2 illustrates the meshes used for the sensitivity analysis, showing that mesh 3 is a good compromise between the number of elements and the element aspect ratio.

Folding of cylindrical composite booms consists of flatting the structure and then rolling it on itself. To investigate the structural behavior associated with these configuration changes, we built two different models. The first model for the study of minimum coil radius was formed by a composite laminate representing the flatten boom, which rolled around a rigid cylinder standing for the hub where the boom coiled (Fig. 3). The coiling radius was set as a parameter and, starting from the value of 15 mm, it was gradually decreased at every analysis. Fig. 3 shows the boundary conditions used in this model. The node set A (on the two edges of the lamina) was free to move in the x-axis and to rotate around the z-axis. The cylinder had a fixed negative displacement u on the z-axis simulating the lamina bending during the rolling process around the cylinder.

The second finite element model was set to investigate the stress fields induced by the flattening process, and consisted of a boom portion of length 20 cm positioned on a rigid plate (Fig. 4). The boom was discretized by 5320 shell elements S4R with reduced-integration scheme. The plate was modeled with 2080 four-node rigid elements, R3D4, which formed a single rigid body connected to a fixed reference node. The simulation of the flattening process consisted of two steps: during the first one, a low pressure was applied on the internal surface of the boom, preventing the rotation of the node sets A and B (Fig. 4) around the x-axis. The second step consisted in the rotation of the node set A around the x-axis, whilst the node set B was fixed and the node set C was prevented from rotating around the z-axis.

2.2 Materials and failure criteria

The laminate considered for the boom structure consisted of ±45 two plies of plain weave made of 1K-T300 carbon fibers, with a linear weight of 7.4 tows/cm in warp and weft directions, and HexPly 913 epoxy resin. The constitutive stiffness matrix was introduced in the finite element model by the command **General Stiffness Section*, which allows to impose directly the ABD matrix (Eq. 1) adopting the values determined by Mallikarachchi [12].

$$ABD^{[\pm 45_2]} = \begin{bmatrix} 7714 & 6380 & 0 & 0 & 0 & 0 \\ 6380 & 7714 & 0 & 0 & 0 & 0 \\ 0 & 0 & 5962 & 0 & 0 & 0 \\ 0 & 0 & 0 & 23.6 & 19.1 & 0 \\ 0 & 0 & 0 & 19.1 & 23.6 & 0 \\ 0 & 0 & 0 & 0 & 0 & 19.9 \end{bmatrix} \tag{1}$$

This approach allows to overcome the limitations of the classical lamination theory (CLT), which is automatically used in the finite element analysis to calculate the composite properties. In fact, CLT lacks in accuracy about the bending properties when ultrathin composite structures are involved [12, 19, 20].

The lamina strength analysis was performed adopting a modified Tsai-Wu failure criterion extended to the force and moment resultants [21]. In particular, the six-dimensional failures were defined by three inequalities as represented in Eq. 2. The first one corresponds to the in-plane failure, the second inequality corresponds to the failure caused by bending loads, and the last one to the failure due to the interactions between the in-plane and bending loads.

$$
\begin{aligned}
&f_1 \cdot \left(N_x + N_y\right) + f_{11} \cdot \left(N_x^2 + N_y^2\right) + f_{12} \cdot N_{xy}^2 < 1 \\
&f_{44} \cdot \max\left(M_x^2, M_y^2\right) + f_{66} \cdot M_{xy}^2 < 1 \\
&\max\left(\frac{N_x}{F_x}, \frac{N_y}{F_y}\right) + \frac{\max\left(\left|M_x\right|, \left|M_y\right|\right)}{F_4} < 1
\end{aligned}
\tag{2}
$$

The coefficients f_I and f_{jk} are defined by equations that are dependent on the ultimate strengths, which need to be determined experimentally [12]. This failure criteria is capable of predicting the laminate failure with higher precision. In Table 2 the laminate ultimate strengths used in this work, previously adopted by one of the authors [16] and determined in [12], are summarized. When in-plane and bending stresses are both present, such criterion can be much more accurate than other used for common laminates. These criteria were introduced in the analysis using a Python script, which computes at the end of the simulation the failure indexes calculation. This approach allows to evaluate each type of load through the laminate section and their interaction, resulting in a continuous optimization process.

3. Buckling analysis

The ultrathin composite boom is a slender structure that needs to withstand the axial loads generating during the operational life. It is well known that this kind of structure shows a failure mode at an actual compressive stress lower than the ultimate compressive stress of the material. Further, the presence of nonlinearities, such as load eccentricity and imperfect nature of structures, contribute to deviate the simulated buckling behavior from the real one. In the case of thin-walled structures, the unavoidable geometrical variations of the thickness due to the composite manufacturing process can have an important role on the real structural behavior. Other imperfections might be evaluated, including load and/or boundaries conditions, which may decrease the value of the linearly predicted buckling load [22]. In this study, such parameters were neglected and we performed a nonlinear buckling analysis using the Riks method on a perturbed model, which was obtained modifying the ideal model by imposing the geometrical imperfections. Such geometrical imperfections were calculated using the local displacements due to the first three eigenmodes obtained by the linear buckling analysis. The local displacements were imposed through the cross-section thickness using the keyword *IMPERFECTION. In particular, different weight factors were adopted and evaluated to scale each eigenmode. This approach consisted in a superimposition of scaled buckling eigenmodes. The imperfections applied were scaled with respect to the thickness of the laminate, using 10%, 20%, 30%, and 100% of the entire wall thickness.

3.1 Results and discussion

Fig. 5 shows the trend of the axial load as a function of the imperfection percentages. The load increases gradually with the axial displacement up to the structural instability. The maximum of the curve is the buckling load for the first mode. With the increasing of the imperfections through the thickness, the instability appears at smaller axial loads. The critical load determined by linear analysis triggered around 55.68 N. On the other hand, in the nonlinear analysis it decreases slightly with the increase of imperfection percentages until it reaches a maximum variation of 4.23% at 100% of geometric imperfections (Table 3). In all cases, a maximum lateral displacement in the central section of the boom with a partial wrapping was observed during the buckling and post-buckling phases. To overcome this phenomenon, we considered the possibility to use a ring, positioned in the center of the boom, to avoid any section displacement. The ring was modeled by two rows of square elements as rigid bodies with respect to a reference node positioned in the cross-section center (Fig. 6).

A post-buckling analysis was performed in order to assess the integrity of the structure after reaching the buckling load. The post-buckling model was processed calculating the failure index FI-3, which considers the axial and in-plane bending moments, giving a clear picture of the possible failure mechanism due to the action of mixed loads. Fig. 7 shows the results of the nonlinear buckling analysis for both boom configurations, where the case without ring is indicated by “default-configuration”. In both cases, the value of the failure index is less than 1, indicating that the structure does not fail. A magnification of the boom centerline in Fig. 8 shows that the additional stresses due to the presence of the ring do not modify substantially the values of the failure index FI-3. Therefore, the laminate will not fail after instability occurs, and it will continue to be safe also during the following post-buckling configuration.

4. Folding simulation

The boom structure is manufactured in its final shape and then packed to be stored in a small volume. The large deformations associated with the folding process induce stress fields that may damage the boom before deployment. In order to investigate the magnitude of these stresses and to evaluate possible failures associated with them, the structural behavior of the boom was studied as composed of two consecutive phases. The boom is initially flattened by imposing an internal pressure and then coiled around an axis orthogonal to its longitudinal direction. To ensure that no material failure occurs during the coiling process, the minimum coil radius was estimated by the laminate strength analysis using a quasi-static explicit method, which eliminates the singularities due to the large displacements [17, 21, 23]. In particular, iterative coiling simulations were performed starting from an initial curvature radius of 15 mm.

The quasi-static explicit analyses are time consuming. To boost up the simulation two main methods can be adopted: the load rates tuning and the mass scaling [24]. The increasing of the load rates may reduce the time needed to complete the analysis, but the increment cannot be randomly chosen. In a quasi-static analysis the dominant response will be generated by the first structural mode. Energy will rise up quickly if the load rate is equal to the actuation frequency of the first mode. This phenomenon causes an increasing of the kinetic energy, thus highlighting the mass inertia which is not relevant for such analysis and therefore needs to be neglected. In order to overcome this issue, the load rate was modified, applying the load with an appropriate amplitude that was included in the "*smooth step*" command. This strategy adopts a fifth order polynomial to generate a modulated loading upon the structure. Commonly, the starting point has amplitude equal to zero, whereas the last point has amplitude value of one, and the time is equal to the total time of simulation. The structure first mode needs to be avoided, otherwise the kinetic energy starts to increase and the quasi-static assumption is compromised. To avoid such unwanted event, the simulation period is taken ten times greater in order to have a good safety factor [20]. Further, the energy may increase at higher frequencies during the load application, causing the unexpected failure of the elements due to large out-of-balance forces that may develop at few nodes. To overcome this problem, a numerical damping given by a bulk viscosity is adopted. Bulk viscosity introduces an in-plane strain-rate dependent pressure p_b (Eq. 3):

$$p_b = \xi \rho c_d l \dot{\varepsilon}_v \tag{3}$$

where ξ is the damping coefficient, ρ is the material density, c_d is the dilatational wave speed, l is the element characteristic length and $\dot{\varepsilon}_v$ is the volumetric strain rate [24]. The linear bulk viscosity coefficient is changed by the default value of 0.06 to a maximum value of 1.8. An additional effective method to introduce a damping factor in the simulation is the viscous pressure load. This method allows damping quickly any instability originated during the simulation without acting on the time increment [17]. This particular load introduces a velocity-dependent normal pressure (Eq. 5) over all elements, and it depends on the viscous constant c_v (Eq. 6):

$$\overline{p} = c_v \cdot \left(v - v_{ref} \right) \cdot \hat{n} \tag{5}$$

$$c_v = \rho \cdot c_d \tag{6}$$

$$c_d = \sqrt{\frac{\hat{\lambda} + 2\hat{\mu}}{\rho}} \tag{7}$$

Where c_v is the viscous constant, c_d is the velocity of the node where the pressure is applied, and $\hat{n}$ is the normal to the element surface. The other parameters are the material density ρ and the Lamè constants $\hat{\lambda}$ and $\hat{\mu}$ [24]. In the present work, the value of the viscous pressure was assumed $p = 2 \times 10^{-4}$ following the literature .

The stability and accuracy of the solution was evaluated by checking the energy balance history, which can be expressed as:

$$E_{tot} = E_i + E_v + E_k - E_w \tag{8}$$

where the total energy E_{tot} is equal to the sum of different energies contribution, i.e. E_i the strain energy, E_v the energy generated by the viscous damping, E_k the kinetic energy and E_w corresponding to the work of all the external forces. In particular, for the quasi-static assumption, the kinetic energy at any simulation increment must be lower than 1% of the internal energy and the energy balance needs to be zero during all the simulation time.

4.1 Results and discussion

The study of the minimum coil radius was conducted by rolling a lamina around a cylinder with fixed radius and analyzing the stresses arising as a consequence of the imposed large deformations. Here we show the results of the quasi-static explicit analysis for cylinders of radius 10 mm and 5 mm. Fig. 9 shows the distribution of the failure index FI-1 of the lamina after the rolling for the two cylinder cases mentioned above. It can be noted that the largest values of the in-plane failure index occur locally in correspondence of the boundaries conditions, but they are always strictly below unity. Fig. 10 illustrates the trend of the failure index FI-2, showing that the structures do not undergo failure due to the bending loads. In both cases, the largest value of the failure index is localized in the central area of the lamina, where the stress field due to the bending moment is maximum. However, it can be noted that FI-2 is significant less than 1 for the coil radius of 10 mm, whereas FI-2 approaches the unity for the coil radius of 5 mm. The failure index FI-3 associated with the combination of in-plane and bending loads shows a similar trend (Fig. 11). In this case, the coil radius of 5 mm shows a maximum FI-3 of 0.95, i.e. the structure is still intact but close to failure. A further reduction of the coil radius will damage the laminate during the first coil.

After determining the minimum coil radius, the folding simulation was considered as composed of two distinct phases, the flattening and the coiling of the boom. The map of the failure indexes at different phases of the flattening step are presented in Fig. 12-14. The values of the failure indexes FI-1 and FI-2 are very small at the beginning (Fig. 12a-13a) and in the middle of the flattening step (Fig. 12b-13b). At the end of the step, when the laminate is completely flatten (Fig. 12c-13c), FI-1 continues to be negligible and FI-2 reaches a maximum value of 0.42 in correspondence of the boundaries, where the bending moments due to the curvature changing mainly act.

As for the other failure indexes, the value of FI-3 is inappreciable at the beginning of the flattening step (Fig. 14a), but it increases while the shape modification progresses (Fig. 14b-c). Therefore, the regions with the maximum value of FI-3 vary from the central area to the lateral edges, coherently with the progress of the elements undergoing the large deformations. However, the value of the failure index always remains below unity, reaching the maximum value of 0.65. Based on these results, it can be assumed that the boom remains intact for the entire flattening step.

Starting from the results obtained for the minimum coil radius analysis, we then studied the stress fields related to the entire coiling step with an initial radius of 5 mm. At the beginning of the rolling, the boom structure shows stress concentrations around the edges in correspondence of the initial wrap, as shown in Fig. 15. These stresses are due to the twisting moments arising from the tendency of the boom section to return in the original configuration contrasting the local change curvature. In order to eliminate these stresses, the folding mechanism has to keep the laminate flat, such as in the case study reported in [17]. For this reason, during the coiling phase the “NODE SET C” (Fig. 4), which contains nodes along the two long boom edges, was constrained in the x-rotation. The results of the structural analysis show that the value of FI-1 sets around 0.062 (Fig. 16) and that of FI-2 at about 0.42 (Fig. 17), indicating that the in-plane loads are less relevant than the bending loads for the entire folding process. According to the previous studies, the coupling of the in-plane and bending loads induces significant stresses, and therefore FI-3 assumes larger values with respect to FI-1 and FI-2. In Fig. 18 we show the distribution of the FI-3 values along the boom structure during three different phases of coiling process: before the coiling, when the boom is completed flat (Fig. 18a); at the first half coil with a radius of 5 mm (Fig. 18b); and after two coils (Fig. 18c). The largest value of the failure index is 0.723 along the elements where the load is applied, hence the boom maintains its structural integrity during the whole folding process.

The solution accuracy was controlled by checking the energy ratio and the energy balance. It is known that the ratio between the internal and the kinetic energies has to be less than 1%, leading to a quasi-static solution, whereas the energy balance has to be constant for all the simulation [11]. Fig. 19 shows the trends of the internal and kinetic energies, and their balance during the entire folding simulation. It can be noted that the internal energy rises up quickly after 0.5 s, and after this instant the kinetic energy is lower than the internal one. The energy balance during the entire simulation remains constantly near zero. The energy balance also includes the artificial energies introduced for the hourglass scheme. At the end of the simulation, which considers the flattening section and a partial coiling, the energy achieved is around 144 N×mm. This represents the stored energy available for the boom deployment. It should be noted that the most important energy gain occurs during the flattening phase, as a direct consequence of the larger change of curvature.

5. Conclusions

In this work, we investigated the structural behavior of a tubular ultrathin composite boom with C-cross section for nanosatellites, focusing on the buckling behavior and the structural integrity during folding. The nonlinear buckling analysis was performed on a perturbed model to verify the effects of the geometrical imperfections on the critical loads and post-buckling behavior. The analysis demonstrated that the proposed boom presents a reasonable axial stiffness, exhibiting a good laminate stability during the post-buckling phase. The critical loads decreased slightly with the increasing of the imperfection percentage, reaching the value of 53 N at 100% of imperfections. On the other hand, a tolerable and more realistic imperfection percentage on composite materials due to manufacturing is around 10% of imperfection variation. Thus, the critical load can be assumed to be about 55 N, which makes this boom configuration an attractive solution for nanosatellites applications.

The post-buckling analysis of the boom highlighted a partial wrapping in the central zone. In order to eliminate such deformation, a simply anti-wrapping system, given by a rigid ring, was evaluated as possible solution. The risk of this approach might be the generation of additional concentration stress around the ring. However, our structural analysis showed that the failure indexes assumed very low values, making this event improbable

Since nanosatellites have limited space available for the hardware, booms need to be stowed in a very small volume. Generally, the base volume is 1 U, i.e. 1 dm^3, so the determination of minimum coil radius and the analysis of the structural behavior during the folding process are important design features. These aspects were investigated using the quasi-static explicit analysis. The smallest radius for the coiling was established to be of 5 mm. The analysis of the failure indexes showed that this dimension guarantees the integrity of the laminate. Similarly, the structural response to the flatting and coiling steps were investigated. In both cases, the most critical loads were the bending moments generated by the change of curvature. The failure indexes values were monitored at different stages of those steps, showing that the proposed boom structure can be flattened and rolled around a small hub without damages of the laminate.

References

[1] Soykasap Ö. Deployment analysis of a self-deployable composite boom. Compos Struct. 2009;89:374-81.
[2] Soykasap Ö, Karakaya Ş. Analysis and testing of ultrathin shell 2□m diameter reflector demonstrator. J Reinf Plast Comp. 2013;32:450-62.
[3] Block J, Straubel M, Wiedemann M. Ultralight deployable booms for solar sails and other large gossamer structures in space. Acta Astronaut. 2011;68:984-92.
[4] Seffen KA, You Z, Pellegrino S. Folding and deployment of curved tape springs. Int J Mech Sci. 2000;42:2055-73.
[5] Puig L, Barton A, Rando N. A review on large deployable structures for astrophysics missions. Acta Astronaut. 2010;67:12-26.
[6] Fetchko P, Sellers JJ. Deployment Optimization of a Boom for FalconSAT-3 Using Elastic Memory Composite Material. Conference on Small Satellites 2004.
[7] Silver M, Dobson B, Warren P. Development of a Deployable Gravity-Gradient Boom CubeSat. 2009 CubeSat Developers' Workshop. Cal Poly, SanLuis Obispo2009.
[8] Mobrem M, Adams D. Lenticular jointed antenna deployment anomaly and resolution onboard the Mars Express Spacecraft. J Spacecraft Rockets. 2009;46:403-10.
[9] Sickinger C, Herbeck L, Breitbach E. Structural engineering on deployable CFRP booms for a solar propelled sailcraft. Acta Astronaut. 2006;58:185-96.
[10] Bamol JA, Murphey TW. Performance Validation of the Triangular Rollable and Collapsible Mast. Small Satellite Conference2010.
[11] Schenk M, Viquerat AD, Seffen KA, Guest SD. Review of Inflatable Booms for Deployable Space Structures: Packing and Rigidization. J Spacecraft Rockets. 2014;51:762-78.
[12] Mallikarachchi HMYC. Thin-walled composite deployable booms with tape-spring hinges [Ph.D. Thesis]: University of Cambridge, 2011.
[13] Leipold M, Eiden M, Garner CE, Herbeck L, Kassing D, Niederstadt T, et al. Solar sail technology development and demonstration. Acta Astronaut. 2003;52:317-26.
[14] Sickinger C. Lightweight deployable booms: design, manufacture, verification and smart material application. 55th International Astronautical Congress, IAF/IAA/IISL. Vancouver, Canada2004.
[15] Laurenzi S, Barbera D, Marchetti M. Buckling design of boom structures by fem analysis. 63rd International Astronautical Congress 2012, IAC 2012. Naples (Italy) 2012. p. 6367-71.
[16] Stabile A, Barbera D, Marchetti M, Laurenzi S. Deployment effects on stability of thin composite boom structures. 17th International Conference on Composite Structures (ICCS17). Porto (Portugal)2013.
[17] Stabile A, Laurenzi S. Coiling dynamic analysis of thin-walled composite deployable boom. Compos Struct. 2014;113:429-36.
[18] SIMULIA. ABAQUS 6.12, Analysis User's manual. Providence, RI2012.
[19] Soykasap Ö. Micromechanical Models for Bending Behaviour of Woven Composite. AIAA/ASME/SCE/AHS/ASC Structures, Structural Dynamics & Materials Conference2005.
[20] Mallikarachchi HMYC, Pellegrino S. Quasi-static folding and deployment of ultrathin composite tape-spring hinges. J Spacecraft Rockets. 2011;49:187-98.
[21] Soykasap Ö. Folding design of composite structures. Compos Struct. 2007;79:280-7.

[22] Simitses GJ. Buckling and postbuckling of imperfect cylindrical shells: A rewiew Appl Mech Rev. 1986;39:1517-24.
[23] Mallikarachchi HMYC, Pellegrino S. Deployment dynamics of composite booms with integral slotted hinges. 50th AIAA/ASME/ASCE/AHS/ASC Structures, Structural Dynamics, and Materials Conference. Palm Springs (CA)2009.
[24] Abaqus I. ABAQUS User Manual. 2010.

Figure captions

Fig. 1. Schematic of boundary conditions for the buckling analysis with detailed view of MPC constraints for the axial loading.

Fig. 2. View of the mesh used to establish the number of elements. a) Mesh1with 10000 S4R elements, b) Mesh 2 with 20000 S4R elements c) Mesh 3 with 25000 S4R elements, d) Mesh 4 with 30000 S4R elements.

Fig. 3. Finite element model for the minimum curvature radius analysis.

Fig. 4. Finite element model used to simulate the folding process.

Fig. 5. Curve of the axial load as a function of the displacement at different imperfection percentages.

Fig. 6. Central ring modelling approach.

Fig. 7. Distribution of the failure index FI-3 in the post-buckling analysis. Default configuration stands for the boom without anti-wrapping ring.

Fig. 8. Details of the FI-3 values in the boom zone with central ring.

Fig. 9. Study of the minimum coil radius: values of failure index FI-1 of the laminate for radius of 10 mm and 5mm.

Fig. 10. Study of the minimum coil radius: values of failure index FI-2 on flattened laminate for radius of 10 mm and 5mm.

Fig. 11. Study of the minimum coil radius: values of failure index FI-3 on flattened laminate for radius of 10 mm and 5mm.

Fig.12. Failure index FI-1 at different flattening stages: a) FI-1 at initial stage; b) FI-1 at middle of flattening step; c) FI-1 when boom is completely flattened.

Fig. 13. Failure index FI-2 at different flattening stages: a) FI-2 at initial stage; b) FI-1 at middle of flattening step; c) FI-2 when boom is completely flattened.

Fig. 14. Failure index FI-3 at different flattening stages: a) FI-3 at initial stage; b) FI-3 at middle of flattening step; c) FI-3 when boom is completely flattened.

Fig. 15. Bending moments due to the tendency of the boom section to return to its original configuration during the coiling step.

Fig. 16. Coiling process. Values of failure index FI-1at different coiling stages: a) initial stage; b) middle of flattening step; c) FI-1 after three coils.

Fig. 17. Coiling process. Values of failure index FI-2at different coiling stages: a) initial stage; b) middle of flattening step; c) FI-2 after three coils.

Fig. 18. Coiling process. Values of failure index FI-3at different coiling stages: a) initial stage; b) middle of flattening step; c) FI-3 after three coils.

Fig. 19. Energy curve during the folding process: the trends of internal, kinetic and balance energy are reported.

List of tables

Table 1. Characteristics of the meshes studied for the finite element model

Model name	mesh1	mesh2	mesh3	mesh4
Number of elements	10000	20000	25000	30000
Critical load [N]	55.51	55.68	55.68	55.68
Computational time [sec]	1160	2250	2780	3480

Table 2. Laminate strength properties

Strength Values	
Tensile, $F_{1t} = F_{2t}$ [N/mm]	139.47
Compressive, $F_{1c} = F_{2c}$ [N/mm]	63.42
Shear, F_3 [N/mm]	17.73
Bending, $F_4 = F_5$ [Nmm/mm]	3.04
Twisting, F_6 [Nmm/mm]	0.92

Table 3. Results of mesh sensitivity

Imperfections %	**Buckling load [N]**	**Difference with respect to linear buckling load**
10%	55.16	0.94%
20%	54.88	1.43%
30%	54.60	1.93%
100%	53.32	4.23%

Figure 1
Click here to download high resolution image

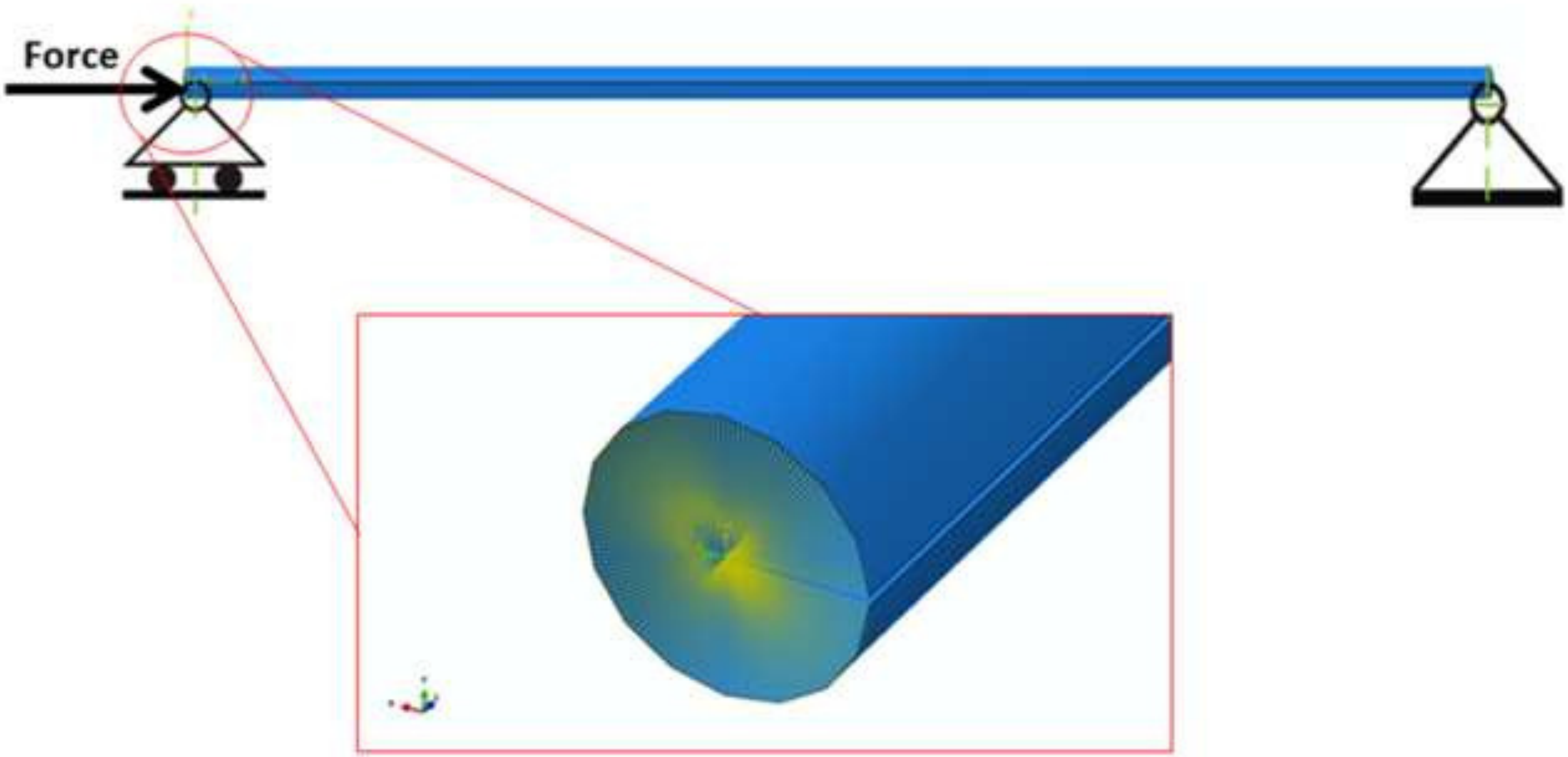

Figure 2
Click here to download high resolution image

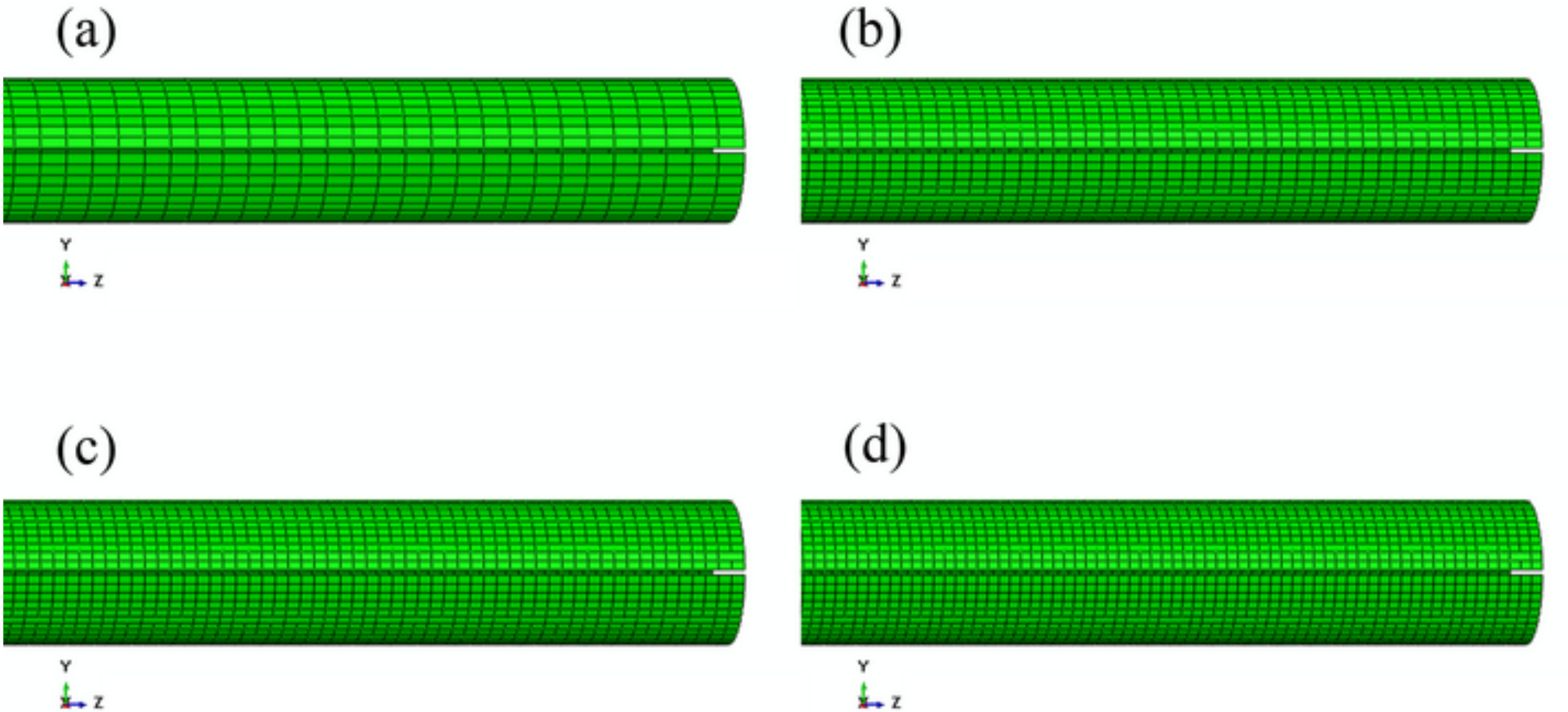

Figure 3
Click here to download high resolution image

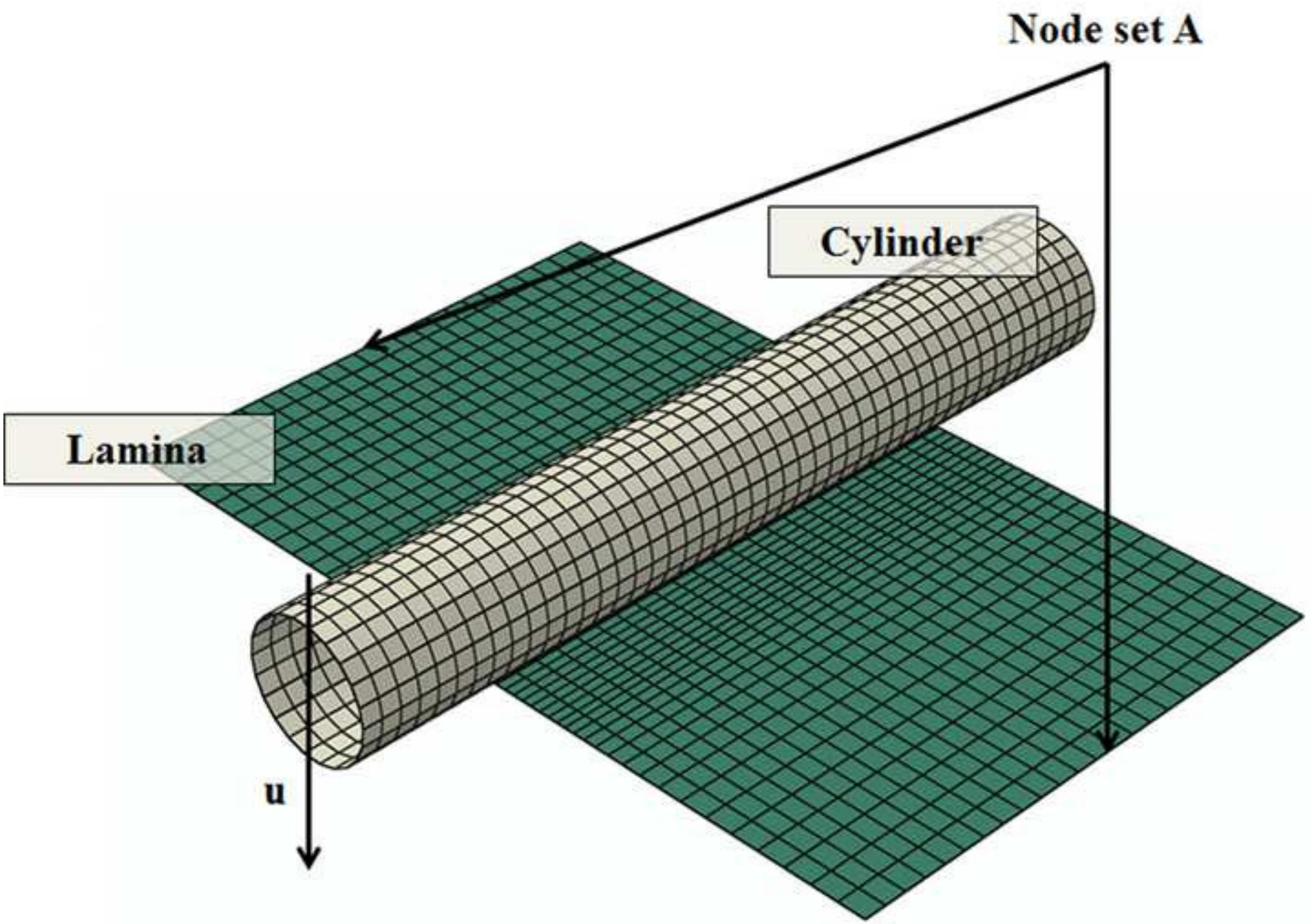

Figure 4
Click here to download high resolution image

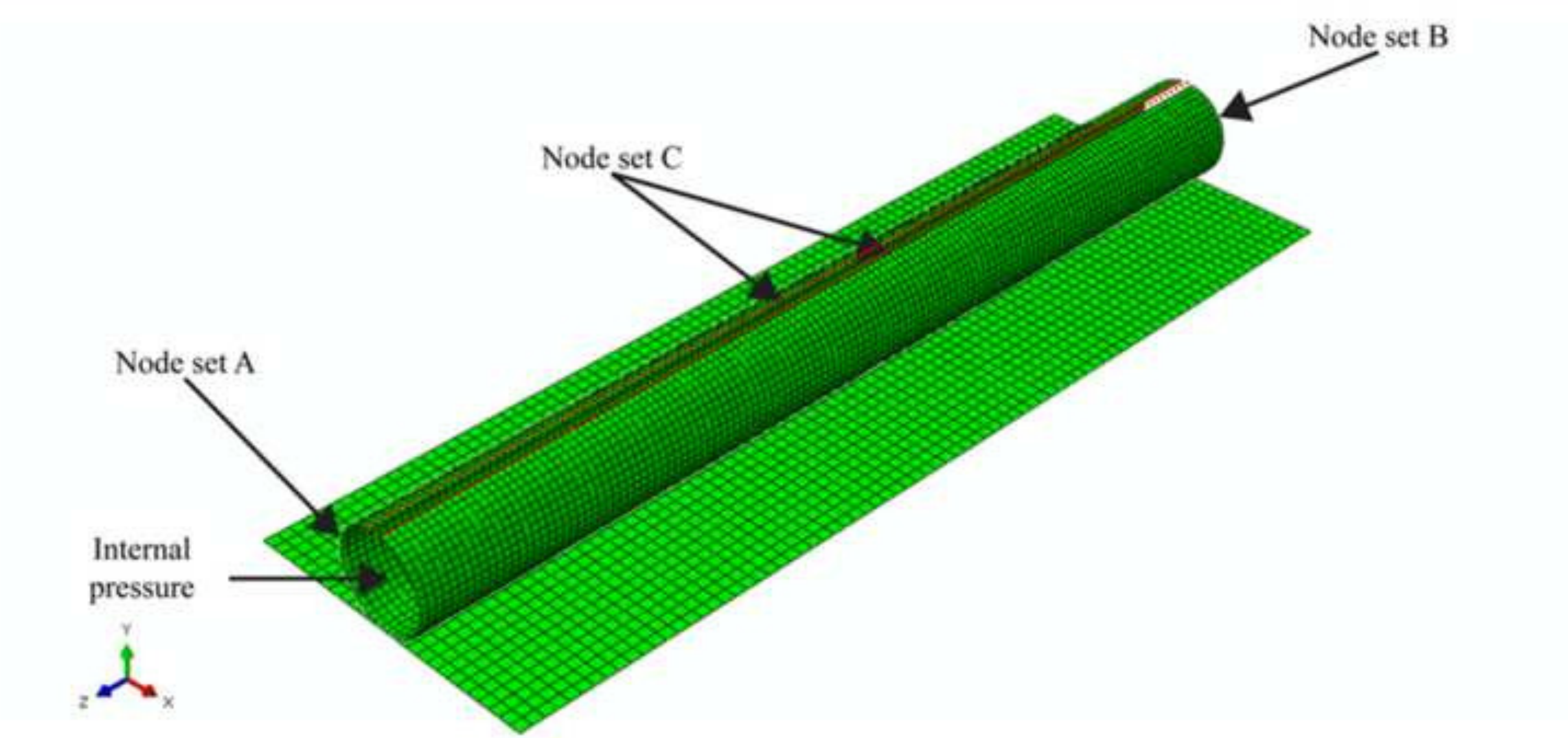

Figure 5
Click here to download high resolution image

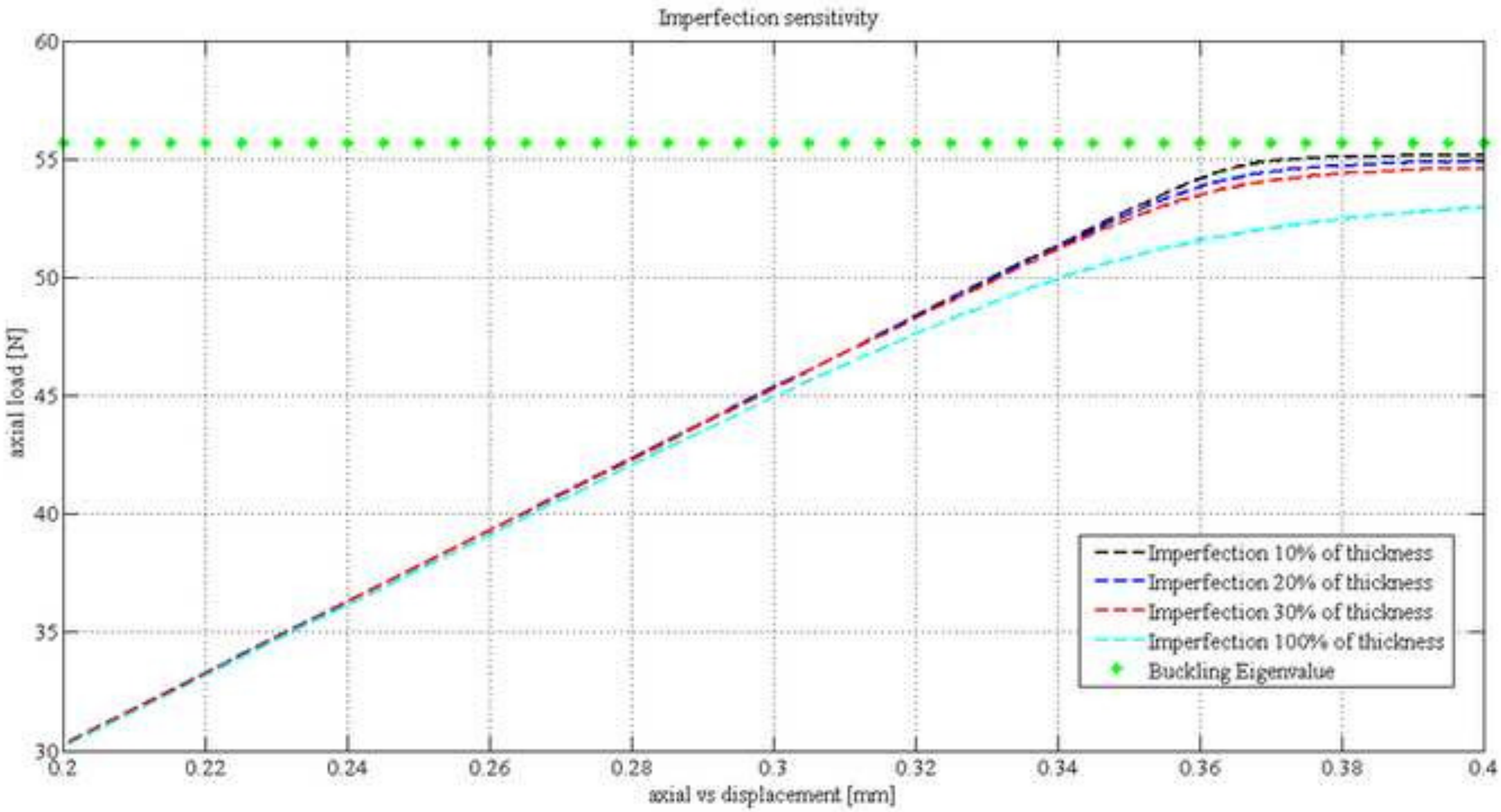

Figure 6
Click here to download high resolution image

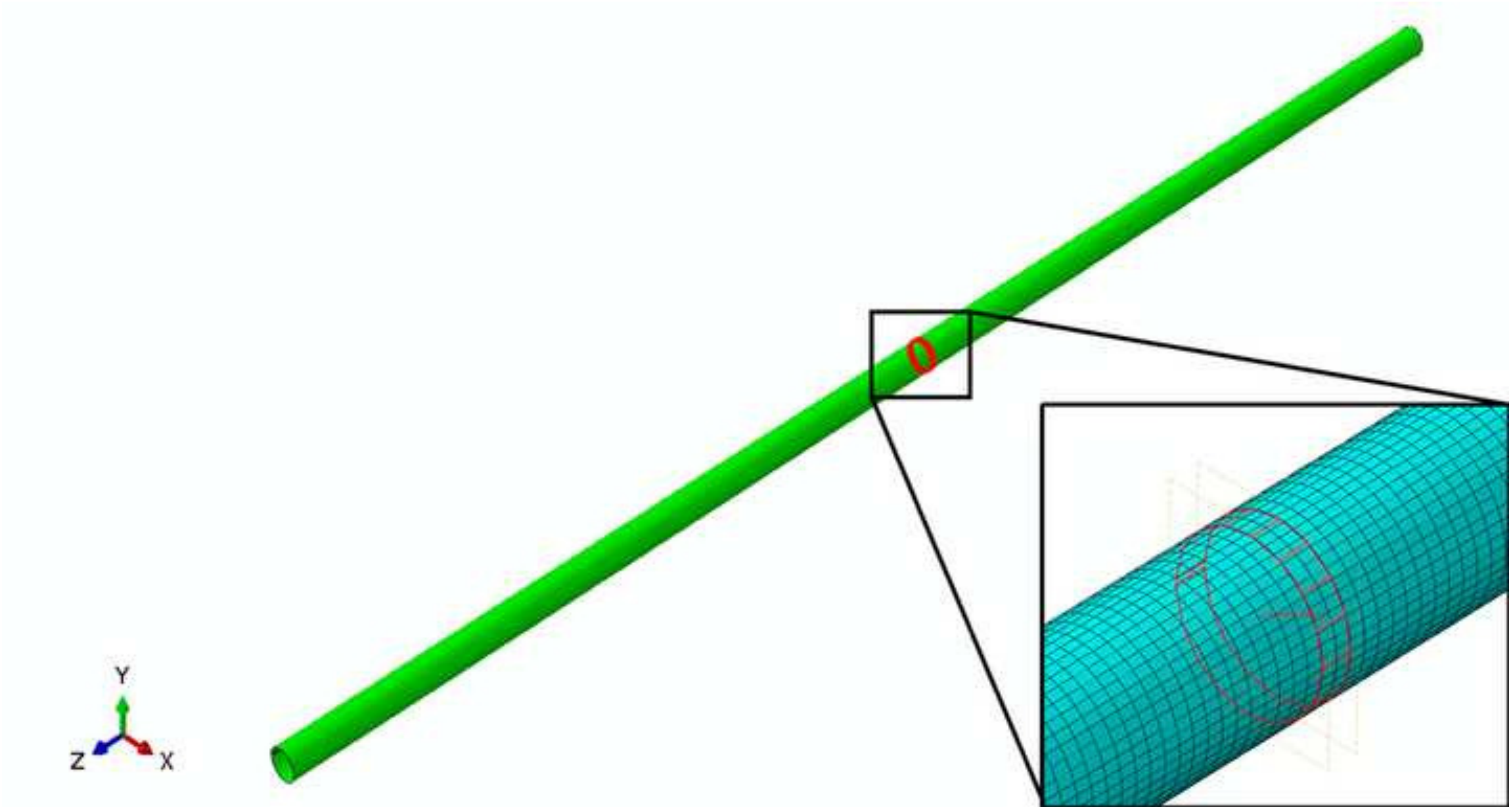

Figure 7
Click here to download high resolution image

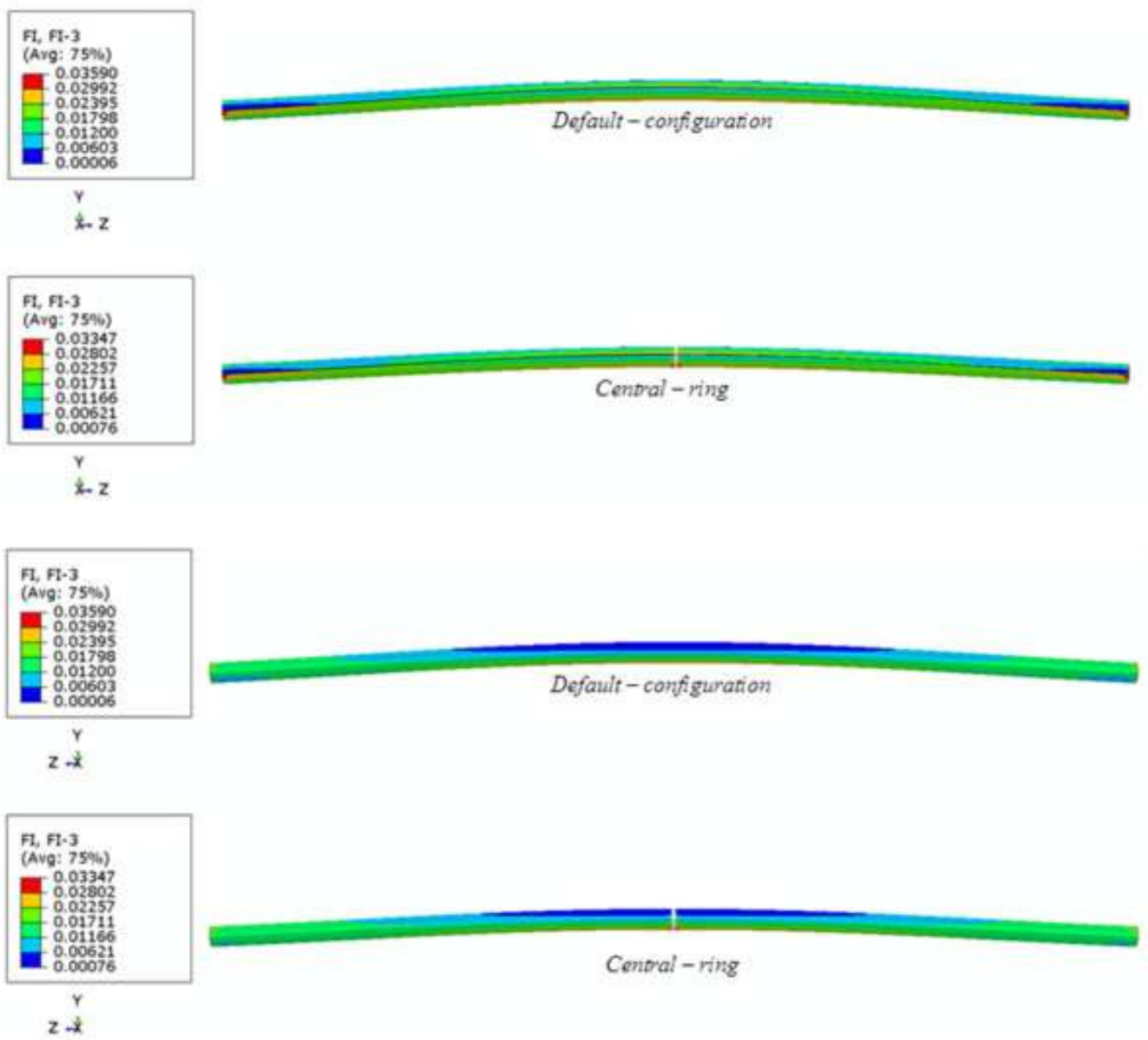

Figure 8
Click here to download high resolution image

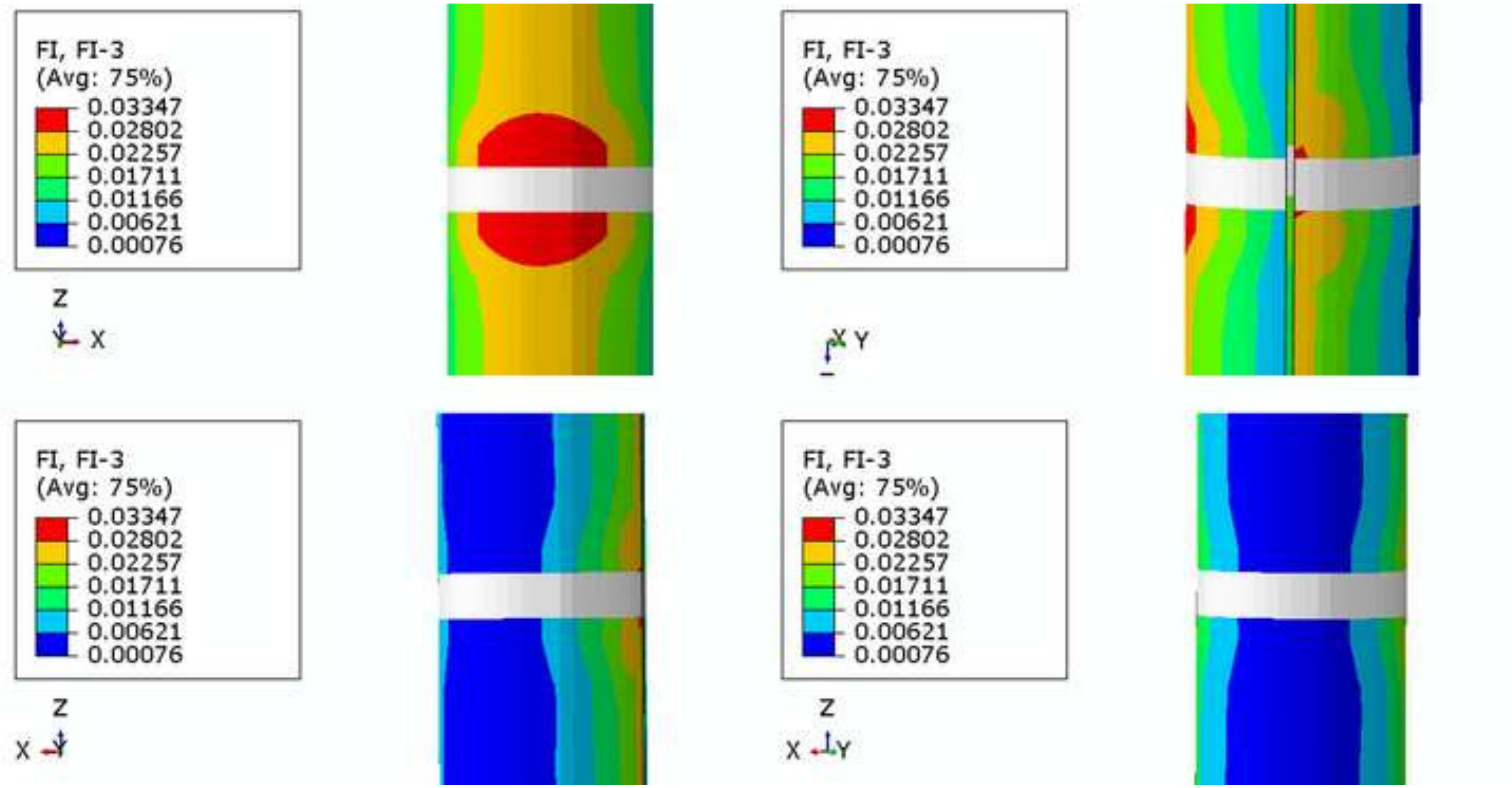

Figure 9

Click here to download high resolution image

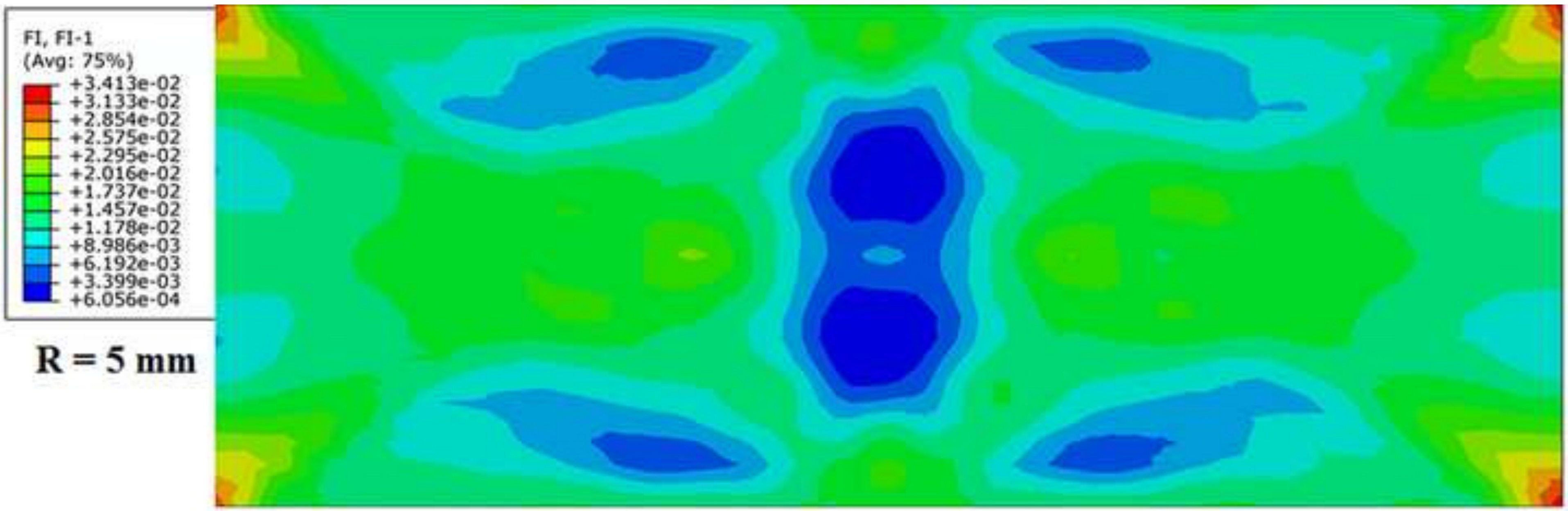

Figure 10
Click here to download high resolution image

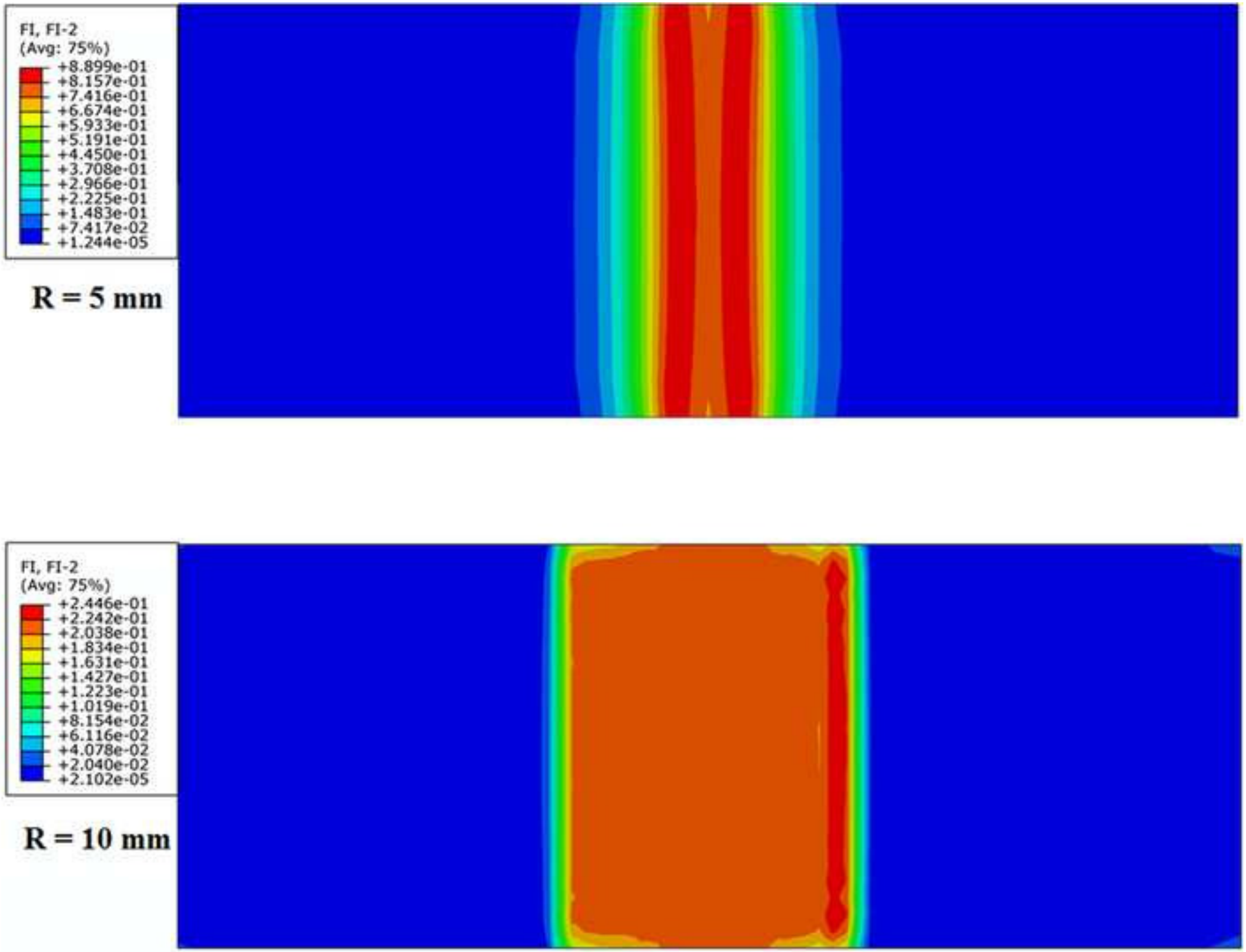

Figure 11

Click here to download high resolution image

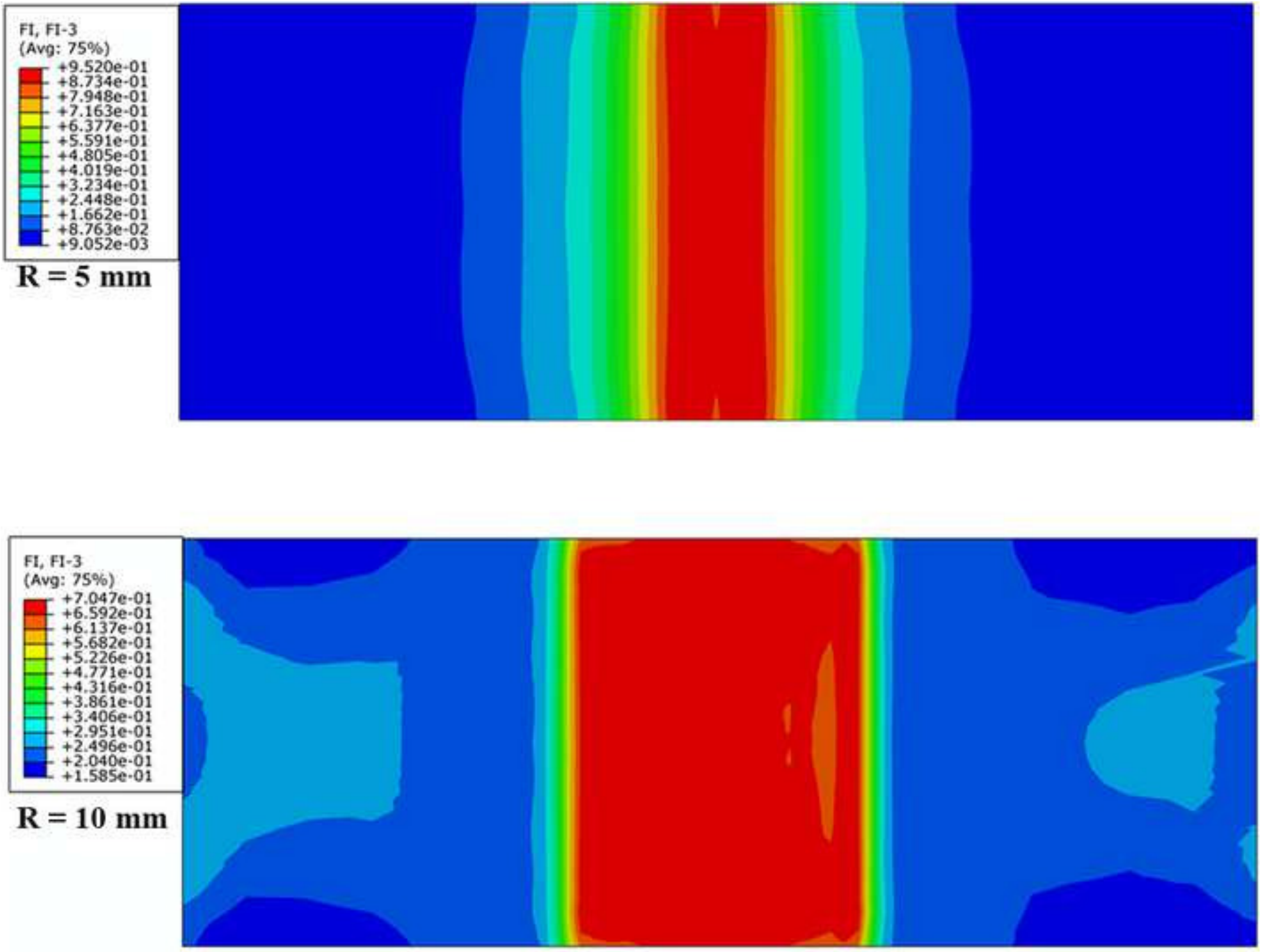

Figure 12

Click here to download high resolution image

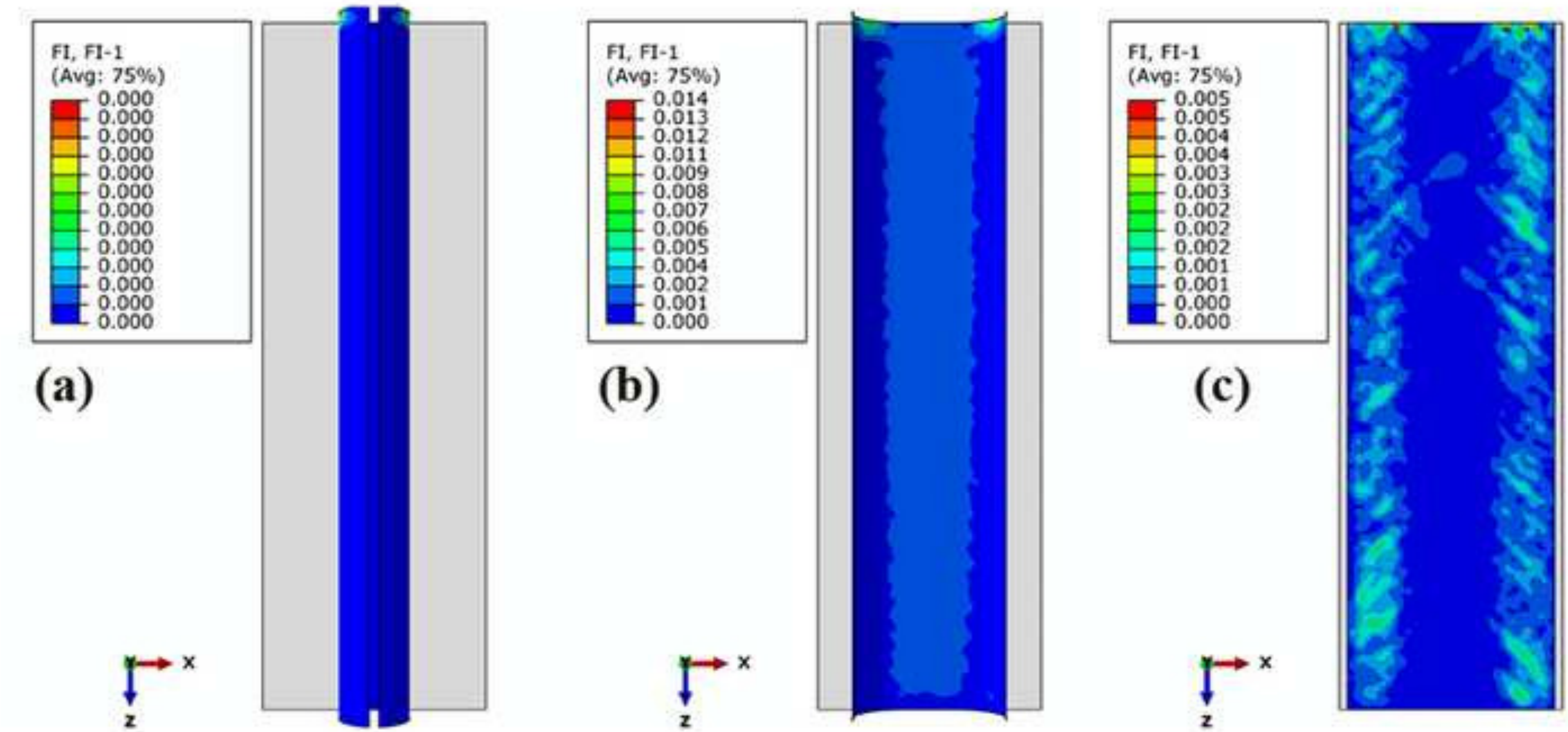

Figure 13
Click here to download high resolution image

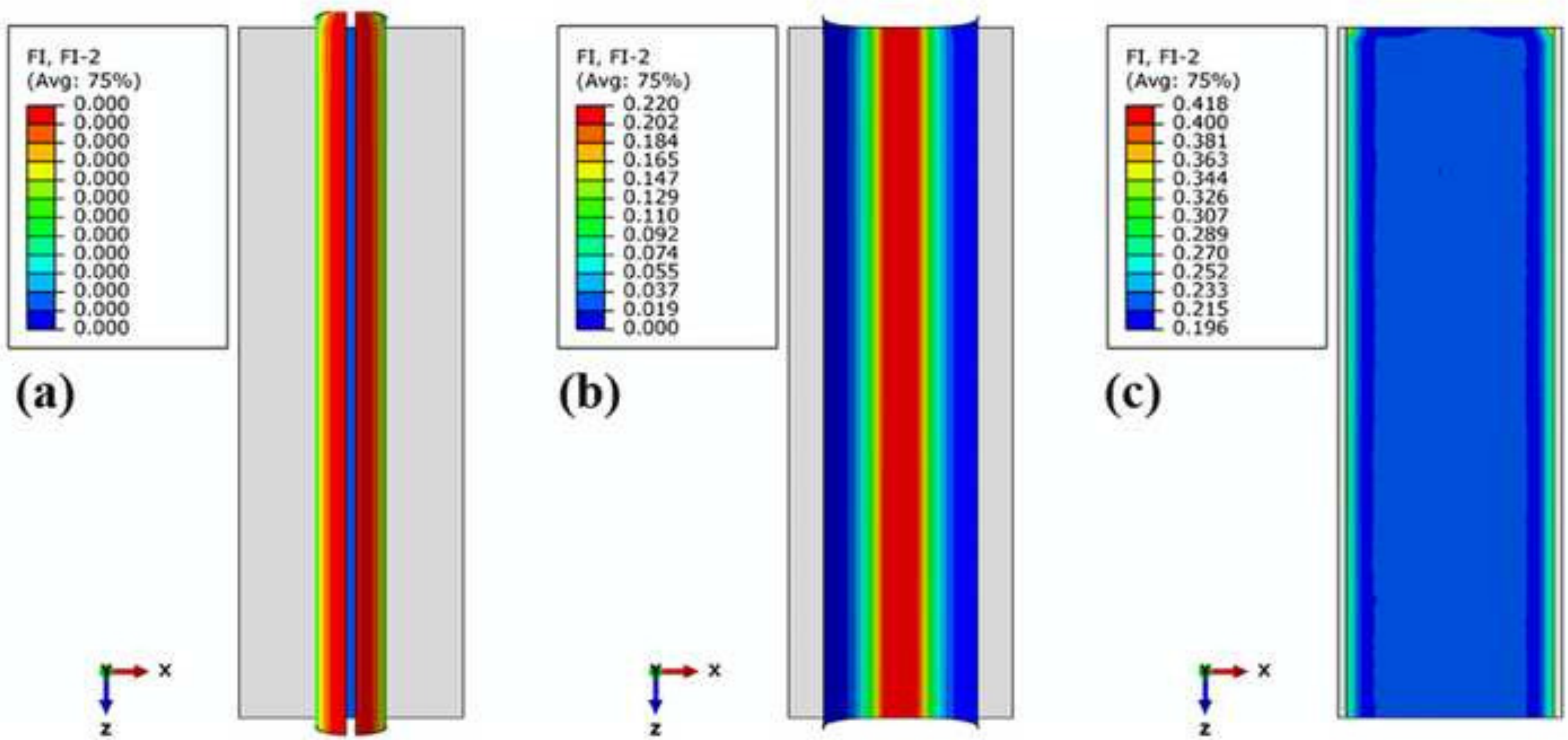

Figure 14
Click here to download high resolution image

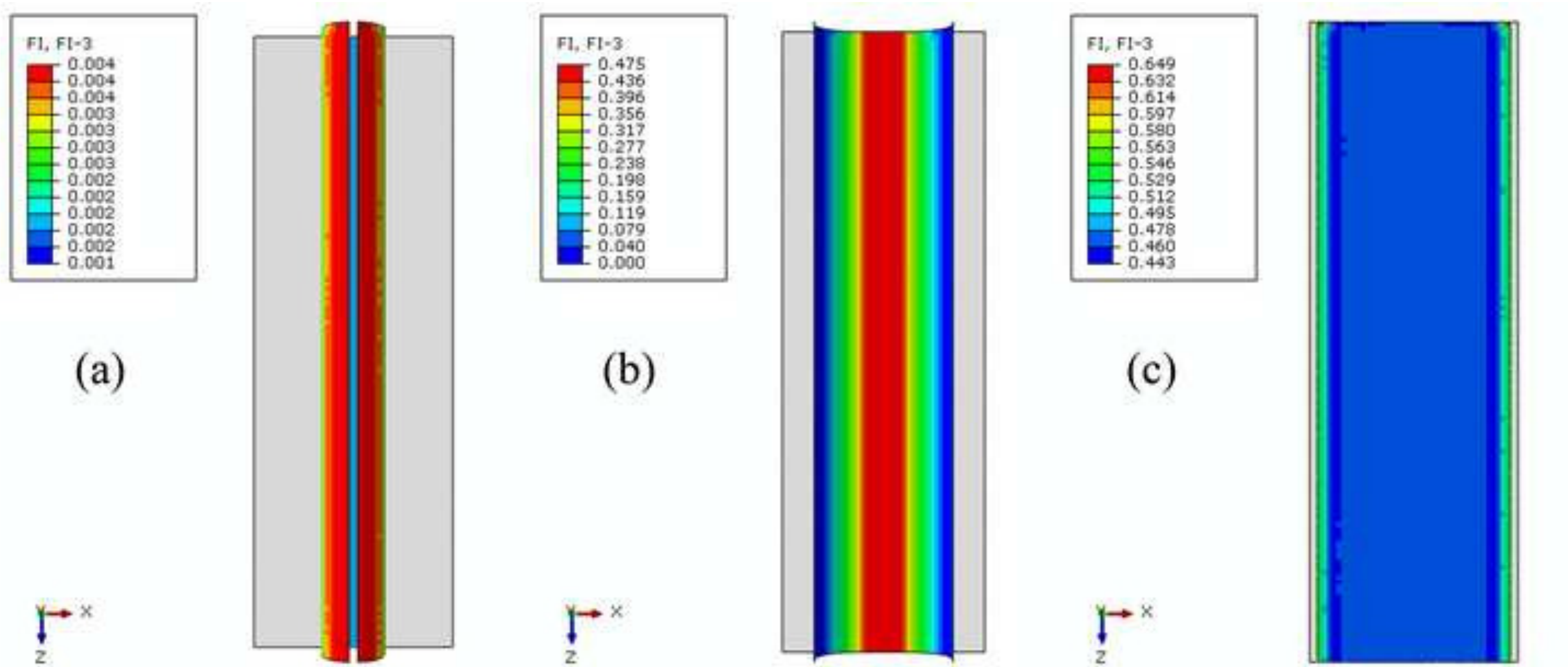

Figure 15

Click here to download high resolution image

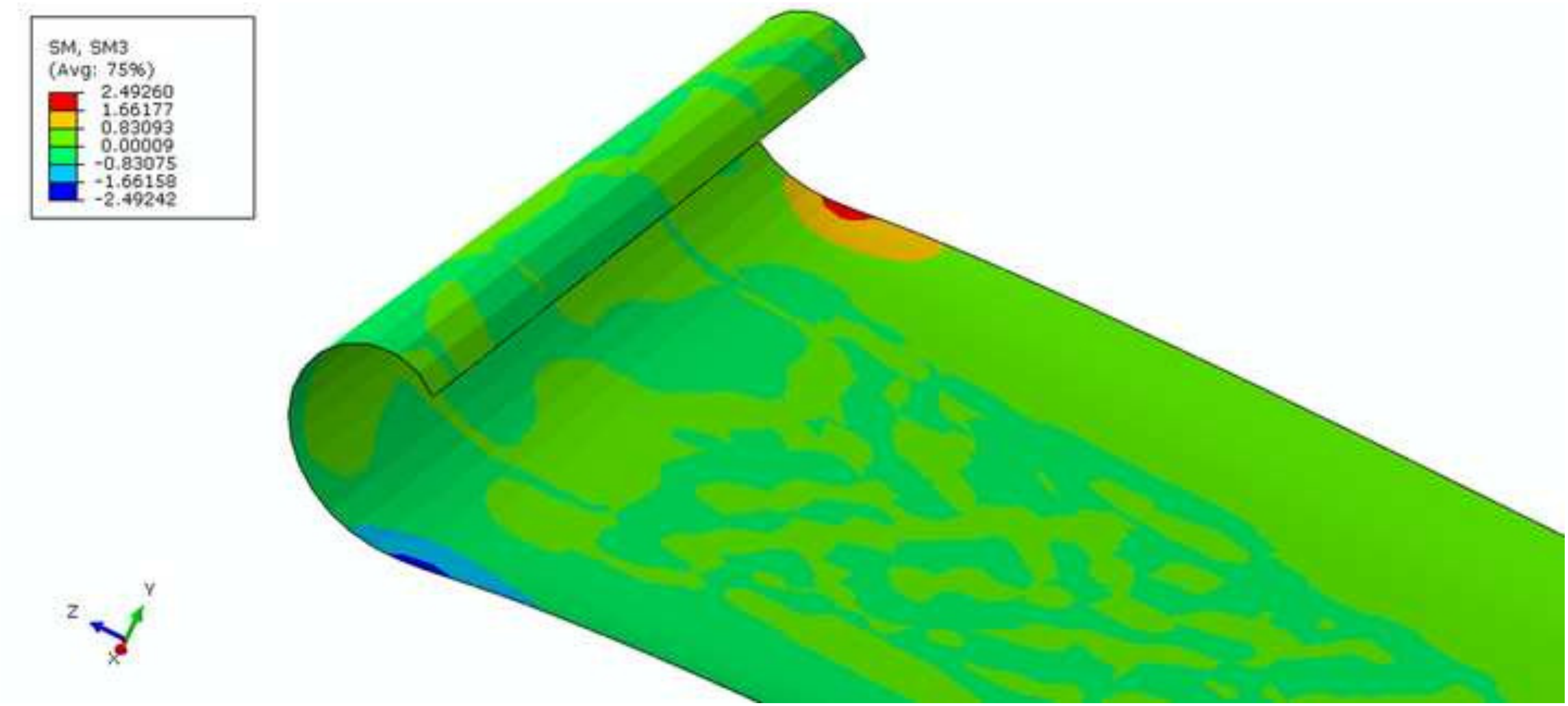

Figure 16
Click here to download high resolution image

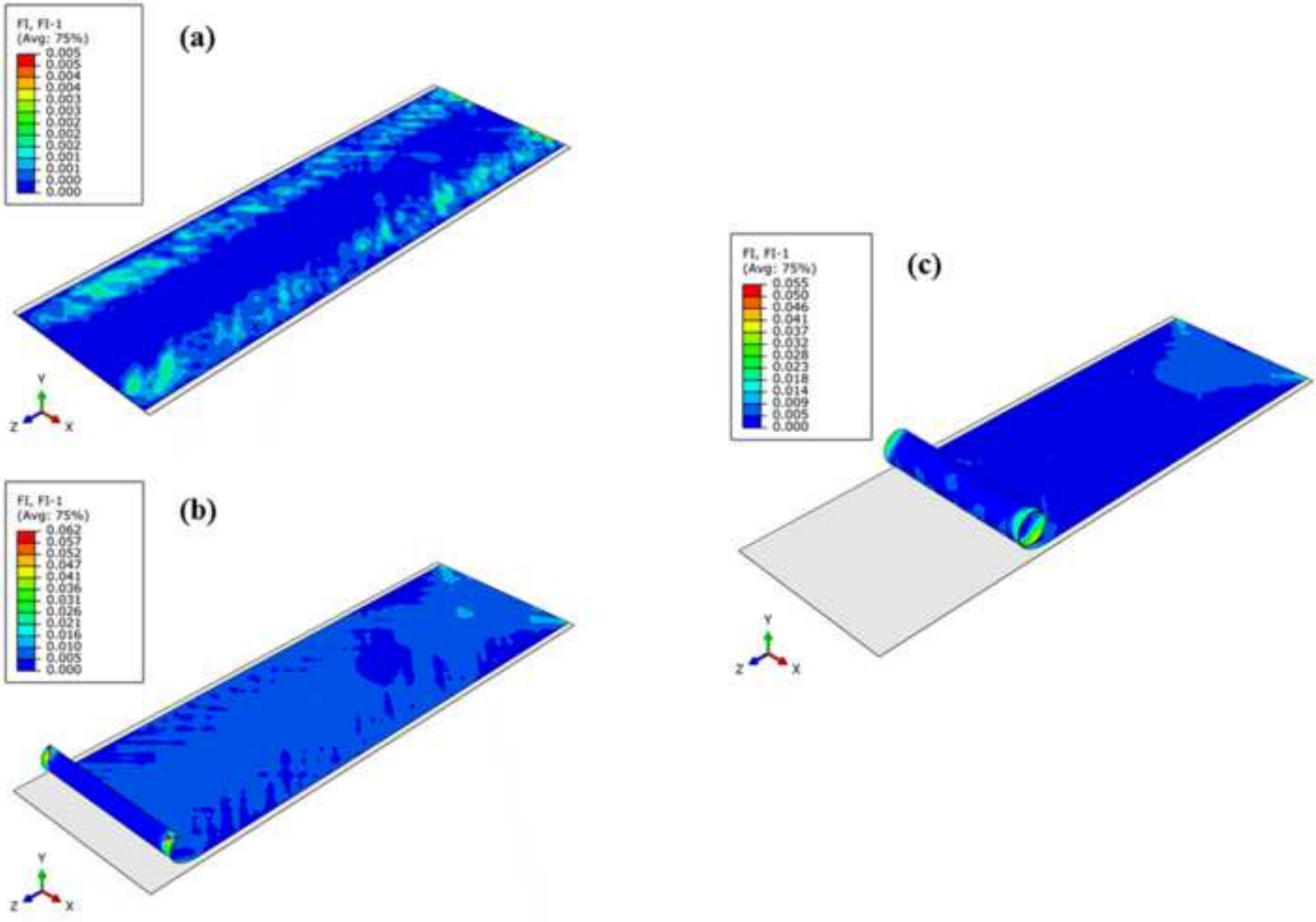

Figure 17
Click here to download high resolution image

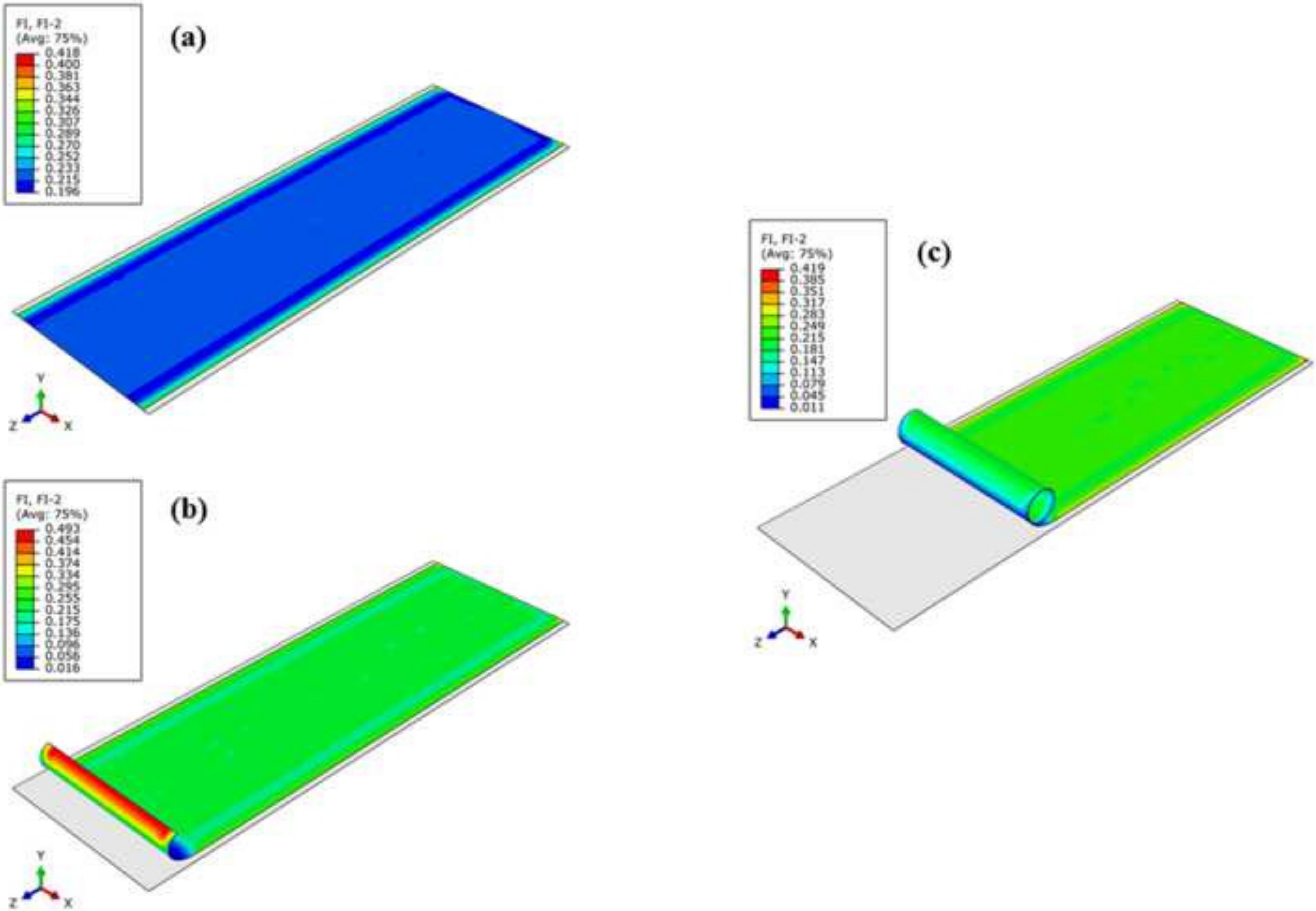

Figure 18
Click here to download high resolution image

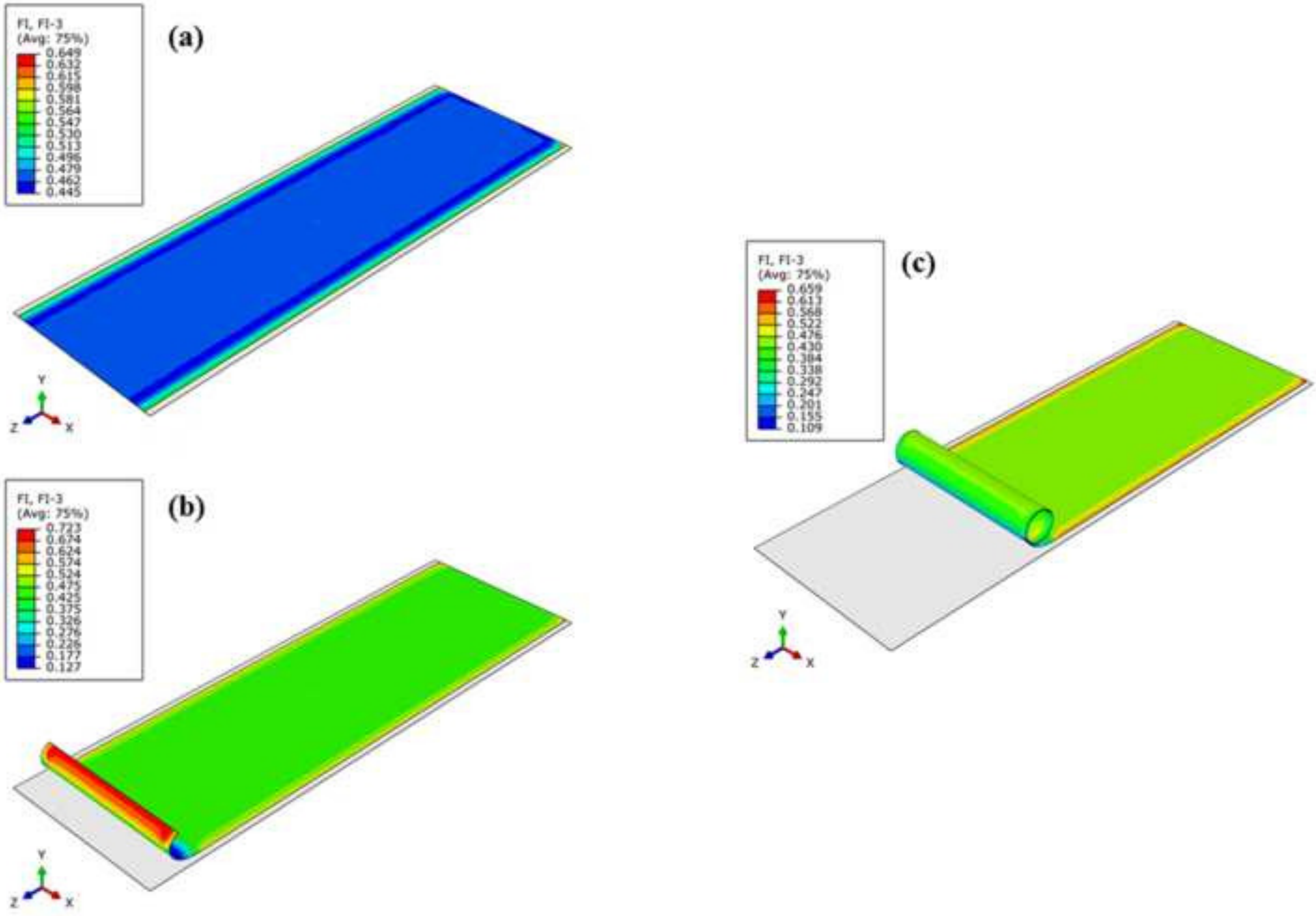

Figure 19
Click here to download high resolution image